THE ASTROPHYSICAL JOURNAL, 438:155–169, 1995 January 1

PLACID STARS AND EXCITED GAS IN NGC 4826[1]

HANS-WALTER R. RIX
Institute for Advanced Study, Princeton, NJ 08540
ROBERT C. KENNICUTT, JR.
Steward Observatory, University of Arizona, Tucson, AZ 85721
ROBERT BRAUN
NFRA, Postbus2, 7990 AA Dwingelo, The Netherlands
AND
RENE A. M. WALTERBOS
Department of Astronomy, New Mexico State University, Las Cruces, NM 88003
Received 1994 May 16; accepted 1994 July 8

ABSTRACT

We present an investigation of the kinematics of the stars and the ionized gas along the principal axes of the galaxy NGC 4826. This galaxy is known to contain two nested, counterrotating, gas disks of a few 10^8 $M_\odot$ each, with the inner disk extending to ~ 1 kpc and the outer disk extending beyond. The stellar kinematics along the major axis, extending across the transition region between the two gas disks, show no hint of velocity reversal or increased velocity dispersion. The stars always rotate in the same sense as the inner gas disk, and thus it is the outer gas disk which "counterrotates." The projected circular velocities inferred from the stellar kinematics and from the H I disks agree to within $\lesssim 10$ km s^{-1}, supporting other evidence that the stellar and gaseous disks are coplanar to $\lesssim 7°$. Using a detailed analysis of the stellar velocity distributions, we can limit the fraction of counterrotating stars in the outer disk to $\lesssim 0.05$, or $\lesssim 2 \times 10^8$ $M_\odot$. This upper limit is comparable to the mass of detected counterrotating gas. This low mass of counterrotating material, combined with the low-velocity dispersion in the stellar disk, implies that NGC 4826 *cannot* be the product of a retrograde merger of galaxies, unless they differed by at least an order of magnitude in mass. The velocities of the ionized gas along the major axis are in agreement with that of the stars for $R < 0.75$ kpc. The subsequent transition toward apparent counterrotation of the ionized gas is spatially well resolved, extending over ~ 0.6 kpc in radius. The kinematics of this region are not symmetric with respect to the galaxy center. On the southeast side there is a significant region in which $v_{\rm proj}$(H II) $\ll v_{\rm circ} \sim 150$ km s^{-1}, but σ(H II) ~ 65 km s^{-1}. The kinematic asymmetries cannot be explained with any stationary dynamical model, even if gas inflow or warps were invoked. The gas in this transition region shows a diffuse spatial structure, strong [N II] and [S II] emission, as well as the high-velocity dispersion. These data present us with the conundrum of explaining a galaxy in which a stellar disk, and two counterrotating H I disks, at smaller and much larger radii, appear in equilibrium and nearly coplanar, yet in which the transition region between the gas disks is not in steady state.

Subject headings: galaxies: individual (NGC 4826) — galaxies: ISM — galaxies: kinematics and dynamics

1. INTRODUCTION

The question of whether all material in galaxy disks has a common sense of rotation has recently attracted considerable attention. In kinematically hot, spheroidal systems, e.g., ellipticals, stars clearly can have different senses of rotation, yielding small net streaming. In contrast, the possibility of significant amounts of counterrotating matter in disks had only been consiered by a few authors (e.g., Toomre 1982; Binney & May 1986). This changed with the discovery of three disk galaxies that contain material of opposite spin: NGC 4550 (Rubin, Graham, & Kenney 1992; Rix et al. 1992), NGC 7217 (Merrifield & Kuijken 1994), and NGC 4826 (Braun, Walterbos, & Kennicutt 1992; Braun et al. 1994; Rubin 1994). The first two galaxies contain cospatial, counterrotating, stellar disks, while NGC 4826 contains an outer H I disk which rotates in the opposite sense to the gas at smaller radii.

These aforementioned examples are quite different from the early-type galaxies containing counterrotating ionized gas (e.g., Bettoni, Galletta, & Osterloo 1991; Bertola, Buson, & Zeilinger 1992) in two respects. First, the counterrotating gas in the latter class is almost confined to the bulge-dominated region of the galaxies; it rarely extends into the galaxy disk. Second, the amount of known gas (10^4–10^5 $M_\odot$) found in these early-type galaxies is lower by a factor of 10^3–10^6 compared to NGC 4550, NGC 7217, and NGC 4826; it constitutes only a tiny fraction of the total disk mass.

Currently no consistent picture of the formation of galaxy disks exists; both the period over which the disk material is assembled and the degree to which this assembly is episodal are under debate. Empirical arguments based on the star formation history of disk galaxies (e.g., Kennicutt 1983) and analytic estimates about late infall into potential wells (Binney & May 1986; Quinn & Binney 1992) suggest that disk gas has been acquired over much of the galaxy's age. In such a scenario, counterrotating disk components, originating from material falling in at different skew angles, are to be expected.

[1] The observations reported here have been obtained with the Multiple Mirror Telescope, a joint facility of the University of Arizona and the Smithsonian Institution.

However, such a scenario of episodic gas acquisition over the life of a galaxy's disk is not borne out by simulations (e.g., Katz 1992), possibly because the initial angular momentum in these simulations is provided by solid body rotation in a "top-hat" overdensity. Also, at the present epoch there is no reservoir of intergalactic H I gas for such infall (Bothun 1985). Therefore, it seems sensible to seek further empirical clues to how galaxy disks are assembled.

This paper is the fourth in a series studying NGC 4826, a galaxy which just may provide such empirical clues (Braun et al. 1992; Braun et al. 1994; Walterbos, Braun, & Kennicutt 1994). These observations have revealed that NGC 4826 contains two distinct gaseous disks: (1) an inner disk ($R < 1$ kpc) of $\sim 10^7\ M_\odot$ in H I and $\sim 10^8\ M_\odot$ in molecular gas; and (2) an outer disk $1.5 < R < 11$ kpc, containing $\sim 10^8\ M_\odot$ in H I which rotates in the opposite sense to the inner gas (Braun et al. 1992, 1994; Casoli & Gerin 1993). Optical photometry shows that most of the light comes from an exponential disk component, with only 20% of the light arising from the bulge (Walterbos et al. 1994). The inner gas disk is coincident with regions of very strong dust lanes, giving the galaxy its nicknames "black eye" or "evil eye" (cf. van Driel & Buta 1993; Witt et al. 1994). When allowance is made for this dust, the underlying disk shows a remarkably smooth exponential luminosity profile, which contrasts with the peculiar structure and kinematics of the gas disk(s). At an assumed distance of 3.8 Mpc, the disk scale length is found to be 1 kpc.

Nonetheless, these observations leave several important questions unanswered. Which way do the bulk of the stars rotate with respect to the inner and outer gas disk? Is there any radius in the disk where stars exhibit cospatial counterstreaming? Is there any other signature of a merger in the disk kinematics, such as increased velocity dispersion? What are the gas kinematics in the transition region between the two gas disks? Some of these questions were answered in a recent paper by Rubin (1994), which presented high-resolution spectra of the Hα and [N II] emission lines at several position angles in NGC 4826. The results confirm the counterrotation in the gas seen in H I and reveal a complex velocity field in the gas in the 1–1.5 kpc transition region. By contrast, the bulk of the underlying Hα stellar absorption lines show normal prograde rotation in the same direction as the *inner* gas disk and show that the outer gas disk is the interloper in NGC 4826 (also see Braun et al. 1994).

We undertook a parallel study of the kinematics of the stars and ionized gas in NGC 4826. The primary goal of our study was to obtain high S/N absorption-line spectra of the stellar disk, in order to accurately measure the rotation properties and velocity dispersion distribution in the disk. By applying the analysis techniques of Rix & White (1992) to these data, we have been able to impose firm limits on the fraction of counterrotating stars in NGC 4826 and constrain the degree of disk heating that would be expected from a large merger event. We have also obtained emission-line velocities in Hβ, [O III], Hα, [N II], and [S II], which allow us to compare the kinematics of the stars and gas on a point-by-point basis. The emission-line ratios, along with detailed spectrophotometry for selected H II regions, allow us to place constraints on the chemical abundances and excitation mechanisms in the gas disks. Taken together these observations allow us to make more informed guesses about the formation history of the object. In particular, we can test whether the counterrotating H I in the outer parts is part of a larger galaxy-galaxy merger or whether only gas has been accreted.

The remainder of the paper is organized as follows: § 2 describes the observations and data reduction, and § 3 details the methodology of kinematic analyses. Sections 4 and 5 present the kinematics of the stars and the ionized gas, respectively. Section 6 discusses the emission-line ratios, and § 7 summarizes the results, focusing on the formation history of NGC 4826

2. OBSERVATIONS AND DATA ANALYSIS

2.1. *Observations*

The data consist of major and minor axis long-slit spectra of NGC 4826, centered at ~5300 Å and Hα (hereafter referred to as the "green" and "red" spectral region). We defined the major axis (P.A. = 125°) by the kinematic fit to the outer H I disk and the minor axis (P.A. = 35°) orthogonal to it. This choice of axies differs by 10° from the ones used by Rubin (1994) and in § 5.2 we discuss the likely location of the (kinematic) principal axes. However, for simplicity we will refer to our choice of position angles as the principal axes throughout the paper. All spectra were obtained on the nights of 1993 April 18–19, using the Red Channel Spectrograph at the Multiple Mirror Telescope. A 1200 gpm grating blazed at 5767 Å was used in combination with a 1".25 × 160" aperture to yield a spectral resolution of ~2.5 Å FWHM. The thinned 1200 × 800 element Loral CCD detector provided a spectral coverage of 950 Å and a spatial sampling of 0".625 pixel^{-1} after on-chip binning. Because of the large apparent size of the galaxy ($D_{25} \sim 10'$), the major axis data were obtained separately for the southeast and northwest side of the galaxy by positioning the galaxy nucleus near either edge of the slit. The total exposure time at each position was split up into separate 20 minute exposures. Separate sky exposures were taken on a nearby piece of blank sky. Twilight sky and quartz lamp spectra were taken for flat-fielding, and each long exposure was bracketed by He-Ne-Ar-Fe arc lamp spectra. Spectra of five stellar templates were obtained with the identical setup, in order to measure the stellar kinematics from the absorption-line spectra centered on 5200 Å. The effective seeing with the stacked MMT image was 0".8–1".3 FWHM during the two nights. A journal of observations is shown in Table 1.

2.2. *Data Reduction*

The initial steps of the data reduction were performed using standard IRAF tasks. These steps included the removal of the CCD bias and dark current, flat-fielding with quartz lamp and sky exposures, and cosmic-ray removal. A transformation from pixel coordinates, $I = I(x, y)$, to wavelength versus slit position

TABLE 1

LOG OF OBSERVATIONS

OBJECT	P.A.	Exposure Time	λ Coverage
NGC 4826 (NW).....	−55°	6 × 1200 s	4690 Å–5690 Å
NGC 4826 (SE)	125	6 × 1200 s	4690 Å–5690 Å
NGC 4826 (minor).....	35	1200 s	4690 Å–5690 Å
NGC 4826 (sky).....	...	2 × 1200 s	4690 Å–5690 Å
HR 3360 (K2 III)	...	~5 s	4690 Å–5690 Å
HR 3641 (G8 II)	...	~5 s	4690 Å–5690 Å
HR 4246 (K3 III)	...	~5 s	4690 Å–5690 Å
HR 5160 (G6 III)	...	~5 s	4690 Å–5690 Å
HR 5219 (K5 III)	...	~5 s	4690 Å–5690 Å
HR 5445 (F5 V).....	...	~5 s	4690 Å–5690 Å
NGC 4826 (NW).....	−55°	3 × 1200 s	6050 Å–6975 Å
NGC 4826 (SE)	125	3 × 1200 s	6050 Å–6975 Å

coordinates, $I = I(\log \lambda, s)$, was calculated using the arc lamp exposures and the traces of the template star spectra. The coordinate transformation, using a fourth order polynomial in each dimension and ~ 500 data points, is well constrained, yielding rms residuals of ~ 0.08 Å in the spectral direction and $\sim 0''.06$ in the spatial direction.

As a final step we constructed a sky spectrum from the two 20 minute exposures off the galaxy (see Table 1), scaled it to match the sky contribution in the galaxy spectra and subtracted it. This procedure was necessary because the galaxy is more extended than the length of the spectrograph slit. Before measuring the galaxy kinematics by comparison with the template spectra, the galaxy spectra were binned spatially to yield approximately constant signal-to-noise per pixel; we chose S/N ~ 40 per pixel. The resulting bins ranged in length from $0''.6$ (1 pixel) in the galactic center to $20''$ in the outermost regions studied ($R = 100''$).

3. DATA ANALYSIS

In the Introduction we posed more ambitious questions about the stellar kinematics in NGC 4826 than are usually asked about *any* external disk galaxy. To answer them, we therefore need to employ more careful and thorough data analysis techniques than conventionally done. We will give a brief summary of the technique used here to study the line-of-sight velocity distribution of the disk stars and the ionized gas. Further details can be found in Rix & White (1992). Readers who are uninterested in the details of the data analysis may proceed directly to § 4.

3.1. *Analyzing the Stellar Velocity Distributions*

The maximum kinematic information one can hope to obtain about the stars at any projected point in the galaxy is a measurement of their line-of-sight velocity distribution (LVD) $f_i(v)$ for all stellar types i. In an ideal situation, this velocity profile is reflected in the galaxy spectrum, $g(\ln \lambda)$, as

$$g(\ln \lambda) = \sum_{\text{all types } i} \int_{-\infty}^{\infty} f_i(v) s_i(\ln \lambda + v/c) dv \, . \quad (1)$$

Here $f_i(v)$ is the probability of finding a star of type i (say, a K giant or an A main-sequence star) at a line-of-sight velocity of v. The spectrum of a template star, Doppler-shifted by v/c, is denoted by $s_i(\ln \lambda + v/c)$.

Note that for observed spectra both sides of equation (1) have been implicitly convolved with the instrumental profile. If an identical setup has been used for observations of both the galaxy and the template spectra and if all spectra are sufficiently sampled, this convolution need not be treated explicitly. For any observed galaxy spectrum, g_o, and any set of template spectra, the "best" velocity profile is defined as the one that minimizes

$$\chi^2 \equiv \| [g_o(\ln \lambda) - g(\ln \lambda)]^2 / \sigma^2(\ln \lambda) \| \, , \quad (2)$$

where $\sigma^2(\ln \lambda)$ is the noise in the galaxy spectrum at the wavelength λ and $g(\ln \lambda)$ is the model galaxy spectrum defined by equation (1).

Several important assumptions are made throughout the literature when estimating $f(v)$, i.e., "measuring the kinematics" of a galaxy, from the galaxy spectrum $g(\ln \lambda)$.

1. The composite stellar population is assumed to consist of only one single, "characteristic" stellar type; this assumption simplifies equation (1) to

$$g(\ln \lambda) = \int_{-\infty}^{\infty} f(v) s(\ln \lambda + v/c) dv \, , \quad (3)$$

where f and s are now luminosity-weighted averages over the stellar mix. Even though the spectrum s will be a composite spectrum, a single star spectrum (e.g., a K giant) is used in most kinematic analyses. This simplification implies that $f_i(v)$ does not depend on the stellar type; it will be discussed more in § 3.2.

2. The LVD is approximated by a Gaussian distribution:

$$f(v) = A \exp\left[\frac{(v - v)^2}{2\sigma^2}\right] .$$

With this assumption the task of measuring the LVD is reduced to determining two discrete parameters, the mean velocity, v, and the dispersion σ. The "best-fitting" parameters (A, v, σ) can then be found using standard nonlinear least-squares fitting algorithms. These assumptions were partly made because of the limited S/N available in the data and partly because they were deemed good approximations to reality.

In the last few years the improved S/N available and new, quantitative analysis techniques (e.g., Rix & White 1992) have allowed us to test these hypotheses. In particular, it was possible to relax the assumption that $f(v)$ is a Gaussian. These studies of more general LVDs have led to the discovery and study of counterrotating stellar disks in NGC 4550 and NGC 7217 (Rubin[2] et al. 1992; Rix et al. 1992; Merrifield & Kuijken 1994). The LVD of cospatial and coplanar counterotating disks is bimodal along the major axis: some fraction of stars have velocities near $+v_{\text{circ}} \sin i$, while the remainder have velocities near $-v_{\text{circ}} \sin i$. Clearly, a simple Gaussian distribution is an insufficient approximation to such an LVD. Rix et al. (1992) used a double Gaussian (DG):

$$f(v) = A_1 \exp\left[\frac{(v - v_1)^2}{2\sigma_1^2}\right] + A_2 \exp\left[\frac{(v - v_2)^2}{2\sigma_2^2}\right] , \quad (4)$$

as a model for the LVD in NGC 4550, with each Gaussian representing one portion of the disk stars.

In our analysis below, we will employ these new techniques to study the stellar kinematics of NGC 4826. In particular, we will use a DG model of the LVD to test whether any stars are counterrotating in NGC 4826.

3.2. *Matching the Stellar Template Spectra*

In addition, we will relax the assumption that the representative stellar spectrum, $s(\ln \lambda)$ is that of a single stellar type. Rather we determine the best composite template spectrum from the data (we will refer to this process as "template matching"). To this end, we first determine the best Gaussian approximation to the LVD, $f_G(v)$ from a fit to the kinematics using a single K giant template. Then we shift and broaden the spectra of a range of stellar types (from A0 V to M0 III) with these kinematic parameters

$$\tilde{s}_i(\ln \lambda) = f_G(v) \otimes s_i(\ln \lambda + v/c) \, , \quad i = 1, M \, , \quad (5)$$

[2] The counterrotation in NGC 4550 was, however, discovered by V. Rubin through visual inspection of long-slit spectra, not through algorithmic analysis of the data.

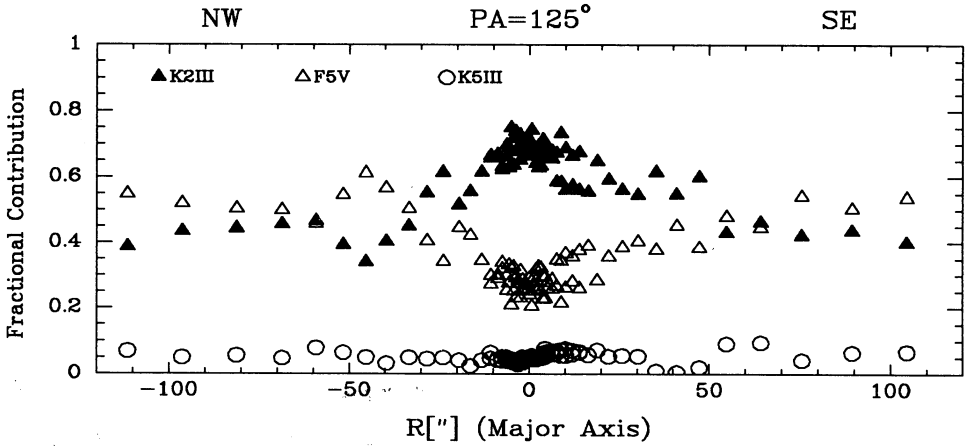

FIG. 1.—Relative contributions of three reference stellar spectra to a "best composite template spectrum" (see eq. [6]) along the major axis of NGC 4826. Inside 50″ the dominant spectrum is an early K giant spectrum, while at larger radii the F main-sequence star spectrum contributes most. These templates fits are purely algebraic and do not consider population synthesis constraints; therefore their implications for stellar population changes are difficult to infer.

where $\otimes$ stands for a convolution. We then find the linear combination of templates, ζ_i which minimizes

$$\chi^2 = \left\| \left[g_0(\ln \lambda) - \sum_1^M \zeta_i \tilde{s}_i(\ln \lambda) \right]^2 \Big/ \sigma^2(\ln \lambda) \right\| . \quad (6)$$

Using these coefficients, ζ_i, we can now assemble the unbroadened composite template

$$s(\ln \lambda) = \sum_1^M \zeta_i s_i(\ln \lambda) \quad (7)$$

to be used in equation (3).

Figure 1 illustrates how the mix of stellar template spectra changes as a function of radius along the major axis of NGC 4826. It shows the relative contributions of a K5 III (*open circles*), a K2 III (*solid triangles*), and a F5 V (*open triangles*) star to the best-fitting template spectrum. It is tempting to interpret the radial gradients in Figure 1, the outward drop in the K2 III contribution and the increase in the F5 V contribution, in terms of population gradients. Even though the change of the mix of template spectra indicates a change in spectral features, interpretation in terms of age or metallicity gradients would be very difficult. It should be stressed that this fit is purely *empirical* and indicates only an outward decrease in the importance of K giant spectral features compared to F5 main-sequence star features.

3.3. *Measuring the Gas Kinematics*

NGC 4826 is classified by Sandage & Tammann (1981) as an Sab galaxy. Consequently, the nebular emission lines are expected to be weak, apart from a few H II regions near the prominent dust lane. The integrated spectrum at most points in the disk is the sum of the stellar absorption-line spectrum and the emission-line spectrum. Since the absorption-line spectrum varies so strongly and rapidly with wavelength, it is difficult to define a "baseline" for weak emission lines. This is illustrated by the top spectrum in Figure 2, which shows the spectral region covering Hβ and [O III] $\lambda\lambda$4959, 5007; at best, the [O III] λ5007 line is barely identified above the background spectrum.

The algorithm described in § 2.1, however, provides a solution to the problem of defining a baseline for the emission-line measurements. To measure the *stellar* kinematics, we fitted a stellar template, composed of various stellar types, to all wavelength regions except the ones where an emission line may be present. Such a best-fitting template spectrum, composed of a F5 V, a K2 III, and a K5 III spectrum, is shown as the broad middle line in Figure 2 (offset by 400 counts from the galaxy spectrum). The quality of the match becomes apparent in the bottom spectrum, representing the difference between the galaxy and the template spectrum. The residuals are almost zero to within statistical errors, except at the wavelengths of the emission lines.

This correction may be problematic for the Balmer emission lines, because the stellar spectra have absorption lines at the same wavelength. However, in most cases where the Balmer absorption becomes strong the emission line is narrower than the broad absorption-line wings; therefore the strength of the Balmer absorption can be determined from the line wings, even

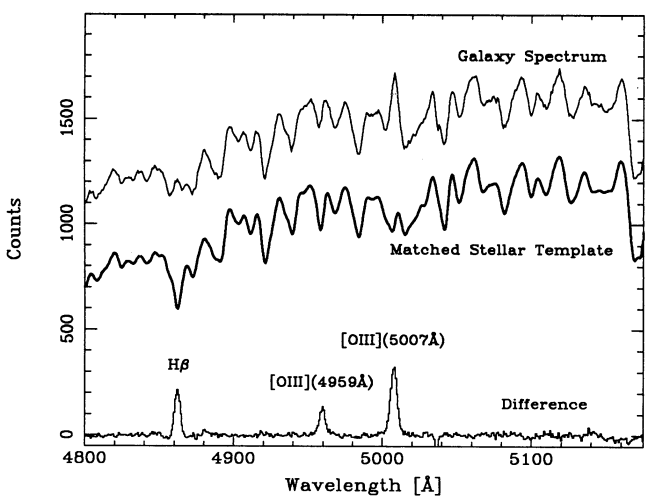

FIG. 2.—Improvement in the measurement of emission-line kinematics and equivalent widths by fitting and subtracting the underlying stellar spectrum. The top line shows the observed spectrum of a region located 5″ off the nucleus along the major axis. Offset by 400 counts, the thicker solid line below shows the matched and broadened stellar template spectrum, derived using eqs. (2) and (6). The bottom plot shows the net difference spectrum. The residuals are zero almost within the noise, except at the wavelengths of the expected emission lines. Note that [O III](4959 Å) is well recovered at its correct ratio to [O III](5007 Å), despite its small equivalent width of ~0.3 Å. Also note the large correction for Hβ absorption.

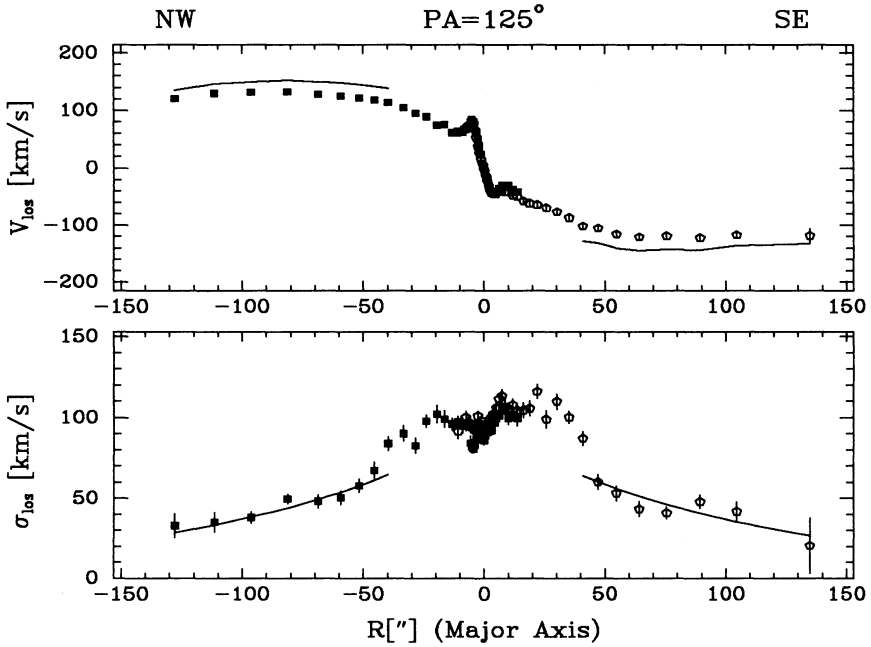

FIG. 3.—The stellar line-of-sight velocity along the major axis (P.A. = 125°) of NGC 4826, derived from a Gaussian fit to the velocity profile (*top panel*). The bottom panel shows the line-of-sight velocity dispersion. The open symbols refer the southeast side of the galaxy, the closed symbols to the northwest side, derived from the separate telescope pointings. Inside 50″, the velocity dispersion profile is significantly asymmetrical, possibly due to dust. Beyond 50″ the velocity dispersions are as low as observed in other disk galaxies. The solid lines in the bottom panel represent a model for σ_ϕ (eq. [8]) fit to the data. The lines in the top panel represent our estimate of the circular velocity, as opposed to the mean streaming motion, v_ϕ, of the stars, accounting for the nonnegligible velocity dispersion of the stars (eq. [10]).

if no weight is given to the line center. All spectra have been corrected for the stellar absorption in this fashion, before measuring the emission-line kinematics in the above fashion. Corrections of this sort are less important for the analysis of Rubin (1994), because she observed only strong emission lines (Hα, [N II]) at higher spectral resolution (~0.7 Å), and because she was interested only in measuring velocities, and not line strengths or ratios.

To increase the S/N, we measured all emission lines within a spectrum simultaneously, forcing them to a common velocity. This constraint was motivated, on the one hand, by the dissipative nature of the cool gas and on the other hand by the empirical evidence that different atomic species usually show very similar kinematics (see, e.g., Rubin's 1994 comparison of [N II] and Hα in NGC 4826). However, Walker (1989) has claimed that in some galaxies the kinematics of different atomic species differ significantly, and our assumption is certainly not beyond further scrutiny. Further, we kept the line ratios for line doublets fixed (e.g., 3:1 for the [O III] doublet), but allowed the line ratios of different elements to vary freely (e.g., the ratio of Hα, [N II], and [S II] in the "red" spectra). All results presented in §§ 5.1 and 5.2 were derived in this way.

When measuring emission-line kinematics, most of the signal comes from only a few points in the recorded spectrum. Consequently, wavelength calibration errors and PSF mismatch might lead to larger systematic errors in V and σ than for the stars. By performing Monte Carlo experiments we found that the minimum velocity error is at least 2 km s^{-1} and the minimum dispersion error is at least $2(\sigma_{\rm inst}/\sigma_{\rm obs})$ km s^{-1}.

4. KINEMATICS OF THE STARS

4.1. *Mean Rotation and Dispersion along the Principal Axes*

Because the H I kinematics of NGC 4826 are so unusual, it is sensible to ask whether the stellar rotation or velocity dispersion are peculiar in any way. We measure the principal axis kinematics by assuming a Gaussian model of $f(v)$ and by minimizing equation (3), using the best composite template spectrum $s(\ln \lambda)$ at each radius. The resulting kinematics along the principal axes are represented in Figures 3 and 4 and are tabulated in Table 3 in the Appendix.

4.1.1. *Major Axis: P.A. = 125°*

The mean line-of-sight velocities show a steep rise in the inner few seconds of arc, with a peak at 2″, then a slow linear rise out to one scale length ($R_{\rm exp} \sim 50''$) and a subsequent flattening. The sense of rotation in the inner parts ($r \lesssim 50''$) is the same as the one of the inner H I disk. This means that it is the *outer* disk that is in counterrotation with respect to the bulk of the stars in the galaxy (Rubin 1994). The stellar rotation curve shows no signature of the reversal which is observed for the gas rotation curve between 50″ and 150″.

Even though it is not evident from Figure 3, the kinematic center of the galaxy does not coincide with the brightest point in the V or R band. By folding the rotation curve in velocity and position, we find that the kinematic center is offset by 0.″95 ± 0.″15 to the northwest with respect to the photometric center.[3] The most straightforward explanation for this phenomenon is that the true galaxy nucleus is obscured by dust. This hypothesis was recently confirmed with K-band images of NGC 4826 obtained by Block et al. (1994), which show a displacement of the apparent nuclei between K and V. Modeling of the dust lane by Witt et al. (1994) shows that the offset is consistent with that expected from extinction effects.

The velocity dispersion also appears asymmetric on either side of the major axis, even after allowing for the offset between kinematic and photometric centers. This is presumably due to

[3] Since this offset is measured along our slit angle of −55°, it corresponds to a offset of 0.″54 to the north and 0.″78 to the west.

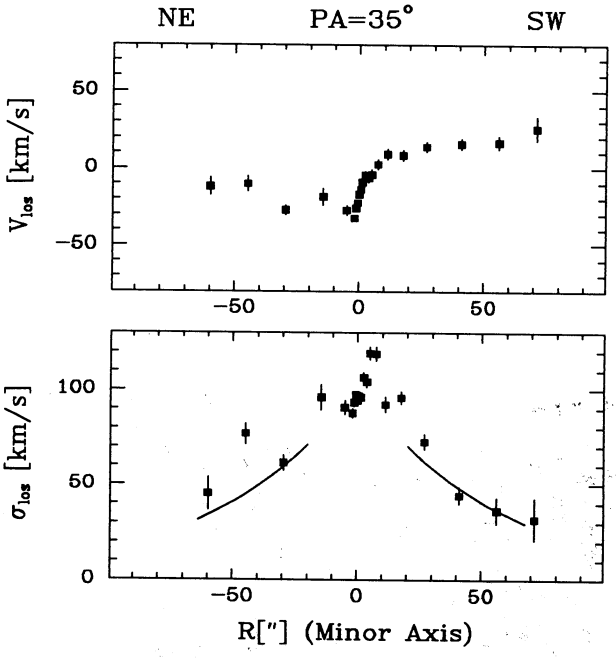

FIG. 4.—The stellar line-of-sight velocity of the stars along the minor axis (*top panel*). The central asymmetries and the dip in the velocities are caused by dust and the resulting offset between the kinematic and photometric galaxy center. At larger radii, $R \gtrsim 15''$, minor axis rotation of ~ 25 km s^{-1} is apparent. The bottom panel shows the minor axis velocity dispersion profile. It is not clear to which extent the erratic behavior of the velocity dispersion on the north-east side is due to the deep dust lanes on this side of the galaxy. The solid lines in that panel represent the dispersion model (eq. [8]) for σ_R, matched to the southwest side of the galaxy and used in calculating the circular velocity from the stellar kinematics.

the presence of dust lanes in the inner parts, which leads to different averages along the line of sight. The stellar dispersion is high (~ 95 km s^{-1}) inside the optical dust lane and then drops steeply to ~ 45 km s^{-1} beyond 50″; this drop is observed on both sides of the galaxy. Its dynamical interpretation, however, may be severely complicated by the dust extinction in the inner parts.

Farther out, between 50″ and 120″, the velocity dispersion drops gently, consistent with observations in other disk galaxies (e.g., Bottema 1993). Indeed, as the bottom panel of Figure 3 shows, beyond 50″ the major axis dispersion profile [$\sim \sigma_\phi(R)$] is well approximated by

$$\sigma_\phi(R) = \sigma_\phi(0) \exp\left(\frac{-R}{2R_{\rm exp}}\right), \tag{8}$$

with $\sigma_\phi(0) = 95$ km s^{-1} and $R_{\rm exp} = 54''$ (Walterbos et al. 1994). Similarly, the minor axis dispersion profile [$\sim \sigma_R(R_{\rm proj}/\cos i)$] can be approximated by the same functional form, but with $\sigma_R(0) = 105$ km s^{-1} (see Fig. 4). At $i \sim 63°$, by NGC 4826 is sufficiently inclined that we can approximate the azimuthal velocity dispersion by the line-of-sight dispersion along the major axis and the radial dispersion by the observed σ along the minor axis. Using the Jeans equation for radial equilibrium, we can estimate the circular velocity v_c from the observed v, σ_R, and σ_ϕ of the stars in this region; this velocity can then be directly compared to H I velocities, assuming $\sigma_{\rm HI} \sim 10$ km s$^{-1} \ll v_c$.

In cylindrical coordinates the Jeans equation for radial hydrostatic equilbrium has the following form (see Binney & Tremaine 1987, eq. [4-33]):

$$v_c^2 = v_\phi^2 + \sigma_\phi^2 - \sigma_R^2 - \frac{R}{\rho}\frac{\partial(\rho\sigma_R^2)}{\partial R} - R\frac{\partial(\overline{v_R v_z})}{\partial z}, \tag{9}$$

where $\rho(R)$ is the luminosity density of the stars and all quantities are assumed to be functions of R. Since the observed light profile and the observed dispersion profiles are well-matched by exponentials (see eq. [8]), we can take the R derivatives in equation (9) analytically, e.g. $\partial\sigma_R^2(R)/\partial R = \sigma_R^2(R)/R_{\rm exp}$. To derive $v_c(R)$, we now need only to assume that the velocity ellipsoid remains aligned in cylindrical coordinates outside of the disk plane, making the last term in equation (9) identically zero; the result is not sensitive to the degree to which this approximation holds. Using this assumption and using the exponential functional forms for $\rho(R)$, $\sigma_R(R)$ and $\sigma_\phi(R)$, we obtain from equation (9)

$$v_c(R) = \sqrt{v_\phi^2 + \sigma_\phi^2 + \sigma_R^2\left(\frac{2R}{R_{\rm exp}} - 1\right)}. \tag{10}$$

The $v_c(R)$, resulting from our major and minor axis data and equation (10), is shown as the solid line in the top panel of Figure 3; it is approximately constant at 142 ± 7 km s^{-1} from 45″ to 130″. For the kinematic inclination of the outer H I disk, $i = 63°$, this corresponds to a velocity of $v_c(\text{stars}) = 159 \pm 8$ km s^{-1}. As we will show in § 5.2, the best estimate for the position angle of the kinematic minor axis (at $R_{\rm maj} \sim 45''$) is about 30°, corresponding to P.A.$_{\rm maj} = 120°$ for an axisymmetric model. If we determined v_c(stars) along a slit position angle which is 5° off the true major axis, v_c(stars) would be reduced by only 1% (see eq. [15] in § 5.2).

This value of v_c(stars) can now be compared to the H I rotation velocity (Braun et al. 1994) along very similar position angles (P.A. $\sim 120°$ and $-60°$) to test the hypothesis that both gas disks and the stars are all coplanar. If an observed velocity difference δv_c between the projected velocities is due to inclinations differing by δi, these quantities are related via

$$\delta i = \frac{\delta v_c}{v_c}\frac{\sin i}{\cos i}\,57.^\circ3\,. \tag{11}$$

For $i = 63°$, $\delta v_c \lesssim 10$ km s^{-1} we find $\delta i \lesssim 7°$. Consequently, we are led to conclude that all the data are consistent with a flat rotation curve and the hypothesis that the stellar disks and the two gas disks are coplanar to within $\lesssim 7°$.

4.1.2. *Minor Axis: P.A.* = 35°

Figure 4 shows the kinematics along the minor axis. The most notable feature of the minor axis rotation curve is a dip at small radii ($\lesssim 3''$). Such a dip is to be expected from the above observation that the brightest part of the galaxy, on which the minor axis spectrum was centered, does not coincide with the kinematic center. Hence at small radii this spectrum samples one side of the velocity gradient along the major axis. At larger radii, the galaxy exhibits significant minor axis rotation, ~ 20 km s^{-1} on the less obscured south-west side. In an axisymmetric model the expected rotation 10° away from the photometric minor axis is only 10 km s^{-1}, or 8% of the major axis value (~ 120 km s^{-1}). This suggests that the galaxy is not perfectly axisymmetric, corroborating the evidence provided by the position angle difference between the kinematic (125°) and photometric (115°) major axes (see Rubin 1994).

In summary, nothing unusual is evident from this analysis of the stellar kinematics of NGC 4826, once the spatial offset

between the kinematic and optical centers of the galaxy are taken into account. It seems that the stars have taken no notice of the peculiar gas kinematics.

4.2. *Are There Counterrotating Stars in the Disk?*

The above analysis of the stellar kinematics does not preclude the possibility that some small fraction δ of the stars in the outer parts of the disk are counterrotating with respect to the majority. Presume that in the center-of-mass velocity frame the true LVD at a major axis point, R, could be well approximated by

$$f(v, R) \propto [1 - \delta(R)] \exp\left[\frac{(v - v_\phi)^2}{2\sigma}\right] + \delta(R) \exp\left[\frac{(v + v_\phi)^2}{2\sigma}\right], \quad (12)$$

as expected for a kinematically cold disk in which the majority of the stars, $1 - \delta(R)$, were rotating approximately at velocity v_ϕ (with a dispersion σ) while the rest, $\delta(R)$, were rotating in the opposite sense, but with the same velocity dispersion.

In a least-squares fit, the best matching single gaussian (eq. [12]) to this LVD becomes *exactly* $\exp[(v - v)^2/2\sigma]$ if $\delta(R) \ll 1$ and $v/\sigma \gtrsim 2$. This means that the second Gaussian (due to counterstreaming stars) may be completely ignored in a conventional kinematic analysis and may not even lead to an increase in the measured velocity dispersion.

We test for the presence of counterrotating stars by using an LVD of the form shown in equation (12). If there were no counterrotating stars we would expect $\langle\delta(R)\rangle \sim 0$. If we force $\delta(R)$ to be nonnegative, we would expect $\langle\delta(R)\rangle \sim \Delta\delta(R)$, where $\Delta\delta(R)$ is the measurement error in the observational estimate of $\delta(R)$. In practice, template mismatch (see, e.g., Rix & White 1992) and imperfect sky subtraction could lead to small, but statistically significant, nonzero values for $\delta(R)$. To reduce the impact of systematic errors, we determine $\delta(R)$ by using the spectra at $+R$ and $-R$ simultaneously, requiring that $f(v, R) = f(-v, -R)$. This antisymmetry will hold for any system that is phase-mixed, i.e., much older than one rotation period. The symmetry of the H I velocity field at larger radii suggests that this condition is fulfilled in NGC 4826.

Figure 5 shows the resulting $\delta(R)$ from a simultaneous fit to spectra from both sides of the major axis. For radii less than 40″, $\delta(R)$ ranges from 0.1 to 0.3, indicating that a sizable fraction of stars has projected velocities which are opposite (in the center-of-mass frame) to the mean streaming. This is expected, given the high-velocity dispersion (bulge and hot disk) in this region, as shown in Figure 3. In a kinematically hot system not *all* stars need to have the same sense of rotation.

At radii beyond ~50″, $\delta(R)$ drops to $\lesssim$0.05, and is consistent with zero beyound $r \sim 80''$. Since $v/\sigma \gtrsim 2$ for $r > 80''$ (Fig. 3), counterstreaming would produce a truly bimodal velocity distribution in this region. Therefore our null result places a strong upper limit on counterstreaming stars $r > 80''$. The formal (1 σ) upper limit on such a fraction $\delta(R)$ is 0.05. This is a limit on the local fraction of luminosity in counterrotating stars (e.g., giants). If this component has a lower mass-to-light ratio, e.g. if it is younger than the underlying prograde disk, then the upper limit on the fractional *mass* of counterrotating stars is more stringent.

The limit on $\delta(R)$ can be converted into a limit on the absolute mass of counterrotating stars which accompany the counterrotating gas in the outer disk ($r > 80''$). Adopting the photometric disk parameters from Walterbos et al. (1994) and assuming a disk mass-to-light ratio of 2.5 in the B band, one finds for the limit on the mass of counterrotating stars, $M_{\rm crs}$, in the outer disk

$$M_{\rm crs} < 2 \times 10^8\, M_\odot \left(\frac{L}{3 \times 10^9\, L_\odot}\right)\left(\frac{M/L}{2.5}\right)\left[\frac{\delta(R > 80'')}{0.05}\right], \quad (13)$$

where L is the total disk luminosity.

This upper limit on the stellar mass is comparable to the lower limit on the counterrotating neutral gas mass in the outer disk: $1.5 \times 10^8\, M_\odot$. Hence at most ~50% of the original gas in the outer (counterrotating) disk has been converted into stars. By contrast the ratio of stars to gas in the prograde disk is ~30, with ~97% of the gas having been converted to stars, a far more typical value for early-type galaxies (Roberts & Haynes 1994). Note that this limit applies only to stars in the plane of the disk; stars with orbits out of the disk plane would not be detected in our spectra.

The apparent absence of counterrotating stars is not surprising given the low surface density of material in the outer disk. Kennicutt (1989) showed that global star formation is suppressed when the local surface density of gas lies well below the Toomre gravitational stability limit $\Sigma = \kappa c/\pi G$, where κ is the epicyclic frequency and c is the velocity dispersion of the gas. Over the radial range $r = 120''$–$500''$ this threshold density ranges over 26–6 $M_\odot$ pc^{-2}, whereas the azimuthally averaged

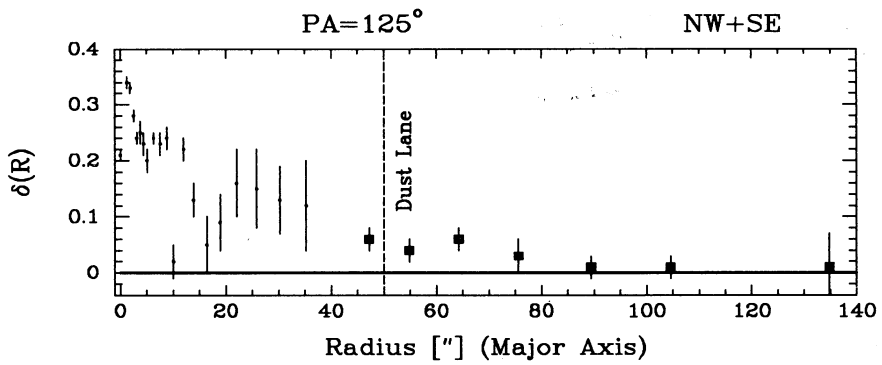

FIG. 5.—Upper limit on the fraction of stars $\delta(R)$ with projected retrograde velocities, as define in eq. (12), as a function of the major axis radial coordinate R. For $R < 40''$, $\delta(R)$ ranges from 0.1 to 0.3, indicating that a sizable fraction of stars has projected velocities which are opposite to the mean streaming. At radii beyond ~50″, $\delta(R)$ drops to $\lesssim$0.05 being mostly consistent with zero. Since $v/\sigma \gtrsim 2$ for $R > 80''$, counterstreaming would lead to a truly bimodal velocity distribution.

H I surface density is $\sim 0.4\ M_\odot\ \mathrm{pc}^{-2}$. At larger radii the discrepancy is even larger. Thus we expect global star formation to be suppressed in the counterrotating disk, and it is quite plausible to speculate that no significant star formation has occurred in the counterrotating system.

5. KINEMATICS OF THE IONIZED GAS

The ionized and neutral gas phases are both dissipational and therefore must have similar kinematics at the same radii if they are to be in a long-lived state at all. The H I measurements (Braun et al. 1994) revealed the spectacular velocity reversal from the inside out, but did not elucidate the detailed structure of the transition region. This was due to both the limited spatial resolution and the low H I surface brightness. Such details could conveivably be provided by the kinematics of the ionized gas. We refer the reader to Rubin (1994) for an excellent analysis of the ionized gas kinematics along P.A. = 90° and P.A. = 25°. Here we briefly discuss the kinematics of the Hβ, [O III], Hα, [N II], and [S II] emission lines in our data, and compare the result to Rubin (1994).

5.1. *Major Axis Kinematics*

Figure 6 shows the mean, projected gas velocities and velocity dispersions along the major axis derived from the various emission lines. The [Hα, N II, S II] data are of considerably higher S/N than the [Hβ, O III] data and are listed in Table 4 in the Appendix. Inside ~40″, the gas velocities are (anti)symmetric about the center and follow the stellar motions. As was the case for the stars, the kinematic center of the ionized gas does not coincide with the brightest point in the V or R band. The offsets found from the stars and the gas are mutually consistent. A significant portion of the central ($R \lesssim 4''$) peak in the velocity dispersion is attributable to the seeing smearing of the steep central velocity gradient.

Outside a radius of 40″ the velocity field of the gas decouples from that of the stars. Here the gas motions show significant asymmetry about either side of the major axis. On the northwest side the gas velocities remain comparable to the star's out to $R \sim 65''$, dropping beyond. On the southeast side, however, the projected velocity of the gas drops smoothly, reaching zero at ~70″. Although the S/N is low, there appears to be hardly any projected rotation from 60″ to 110″ along P.A. = 125°. This "transition region" appears smooth and is spatially well resolved, extending over ~600 pc. However, as the bottom panel of Figure 6 shows, the projected velocity dispersion of the ionized gas in this region varies from 50 km s^{-1} to 75 km s^{-1}. This is much higher than the $\lesssim$20 km s^{-1} that is usually found in H II regions and other cold gas components, but is not as high as the value required to provide full hydrostatic support for the gas, $v_{\mathrm{circ}}/2^{1/2} \sim 110$ km s^{-1}. On the north-west side, where $v \sim 130$ km s^{-1} from 40″ to 70″, the velocity dispersions are low. These data clearly show that (*a*) the projected gas kinematics (v and σ) in the transition region are not symmetric about the galaxy center and that (*b*) the gas velocity dispersion contributes significantly to the hydrostatic support of the gas in the transition region. A plausible mechanism for these large

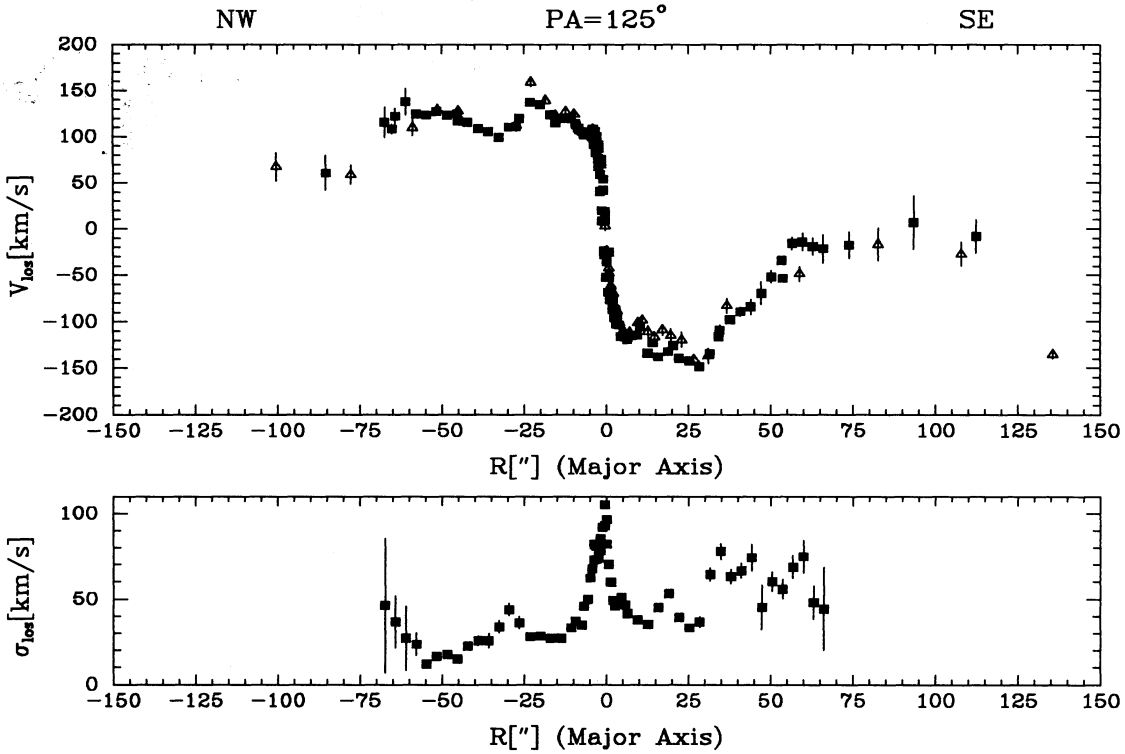

FIG. 6.—Line-of-sight velocities and dispersions of the ionized gas along the major axis (P.A. = 125°). The open symbols denote velocities derived from Hβ and [O III], the filled symbols denote the Hα, [N II], and [S II] velocities. At radii less than 40″ the velocities are reflection symmetric with respect to the galaxy center, but not beyond. While on the southeast side there is an extended smooth change in velocity reaching the center-of-mass velocity at +60″, no such change is observed at the same radii in the northwest. Only at radii $R \gtrsim 70''$ is there evidence for a transition region in the north-west. The measurement at $R = +135''$ might be due to a planetary nebula in the stellar disk. Similarly, the velocity disperson profiles are asymmetric for $R \gtrsim 40''$, barely resolved ($\sigma \lesssim 20$ km s^{-1}) lines in the northwest contrast with ~70 km s^{-1} in the transition region in the southeast side. The central velocity dispersion peak is partly due to the seeing smearing of the steep velocity gradient seen in the top panel.

line widths (and the line ratios, see § 6.1) may be gas heating by shocks. It is worth noting that the observed kinematic asymmetries cannot be explained by steady state models, even if we were to invoke inflow, warps, or elliptical orbits. All these phenomena produce intrinsic velocity fields which have odd symmetry, $v(r) = -v(-r)$. This symmetry is preserved under projection, $v_{\rm proj}(r_{\rm proj}) = -v_{\rm proj}(-r_{\rm proj})$, but not satisfied by our data.

Qualitatively similar features can be seen in the data derived by Rubin (1994) from the deeper spectrum in the east to west direction (25° from the major axis), but the detailed velocity field is different from that we observe along the major axis. The east to west data show that velocity transition continues farther to the east, reaching the circular velocity (but retrograde) at $r \sim 100''$, which would correspond to $r \sim 130''$ along the major axis. The different kinematics along P.A. = 90° and P.A. = 125° may not be surprising considering that the kinematics along any fixed P.A. are not symmetric and considering the H I velocity field at these radii cannot be fitted with a simple tilted ring model.

5.2. *Minor Axis Kinematics*

The mean line-of-sight velocities of the ionized gas along the minor axis are shown in Figure 7. No "red" spectra were taken at this position angle, and hence all information is derived from Hβ and O III. At most radial points the S/N was insufficient to derive velocity dispersions; therefore only the velocities are listed in Table 4 of the Appendix.

As in the case of the stellar kinematics, this central "dip" is to be expected from the offset between the brightest part of the galaxy and its kinematic center. The dip is more pronounced than for the stars, because this spectrum samples one side of the much steeper velocity gradient in the ionized gas.

At projected distances between 5″ and 40″, corresponding to 10″ to 80″ along the major axis, the data show a small amount of minor axis rotation, ~20 km s^{-1}, quite comparable to that seen in the stars. Finally, the one data point at $\sim -50''$ is a solid measurement. If interpreted in a coplanar geometry, it would correspond to a radial (or inflow) velocity of ~85 km s^{-1}. This point corresponds to an extended high-velocity feature over $r = 30''$–$60''$ detected by Rubin (1994). We refer the reader to that paper for further discussion of what appears to be minor axis infall in NGC 4826.

At minor axis distances of 15″–30″, where the kinematics appear regular, we can combine the data of Rubin (1994) along −16° and 25° with our data along 35° to obtain an improved estimate of the kinematic minor axis. Presume that the ionized gas is on closed orbits in an axisymmetric disk at inclination i with a major axis position angle of P.A.$_{\rm maj}$ and a rotation curve $v_c(R) \equiv v_c^0(R)\sin i$. A point at a projected distance R' at a (projected) angle $\theta_{\rm P.A._m} = -$ P.A.$_{\rm maj}$ from the major axis has a deprojected distance of

$$R = R'\sqrt{1 + \sin^2(\theta_{\rm P.A._m})\tan^2(i)}\,. \quad (14)$$

The line-of-sight velocity at that point $[R', \theta_{\rm P.A._m}]$ is given by

$$v_{\rm los} = v_c(R)\cos\theta_{\rm P.A._m}/\sqrt{1 + \sin^2(\theta_{\rm P.A._m})\tan^2(i)}\,. \quad (15)$$

We adopt $v_{\rm los}(-16°) = 70$ km s^{-1}, $v_{\rm los}(25°) = 0$ km s^{-1} (Rubin 1994) and $v_{\rm los}(35°) = -15$ km s^{-1} (this paper) at projected distances of ~25″, and combine this input with the major axis velocity at $R \sim 40''$ (from P.A. = 115° [Rubin 1994] and P.A. = 125° [this paper]) of ~145 km s^{-1}. Then we vary P.A.$_{\rm maj}$ to match the velocities near the minor axis and find P.A.$_{\rm maj} = 120° \pm 5°$, or P.A.$_{\rm min} = 30° \pm 5°$, intermediate between the values advocated previously. However, it must be noted that no axisymmetric model can match the data at all six position angles (−16°, 25°, 35°, 90°, 115°, 125°) satisfactorily, providing further evidence that the kinematics of this galaxy are not quite axisymmetric.

6. LINE RATIOS OF THE IONIZED GAS

6.1. *Disk Gas*

Emission-line ratios can be used to constrain the excitation mechanisms and chemical abundances in the gas. These in turn provide some quantitative constraints on the evolution of the disk. Two sources of information are available: (1) A string of H II regions is present near the northeast dust lane (for an Hα image see Rubin 1994). Oey & Kennicutt (1993) obtained spectrophotometry in the 3727–5007 Å region for five of these H II regions, and additional spectra in Hα, [N II], and [S II] were obtained during our observing run. (2) Our red major axis spectra provide information on the [N II]/Hα and [S II]/Hα ratios in the diffuse gas. Although information on [O III] and Hβ in the diffuse gas is also available, we have not analyzed the

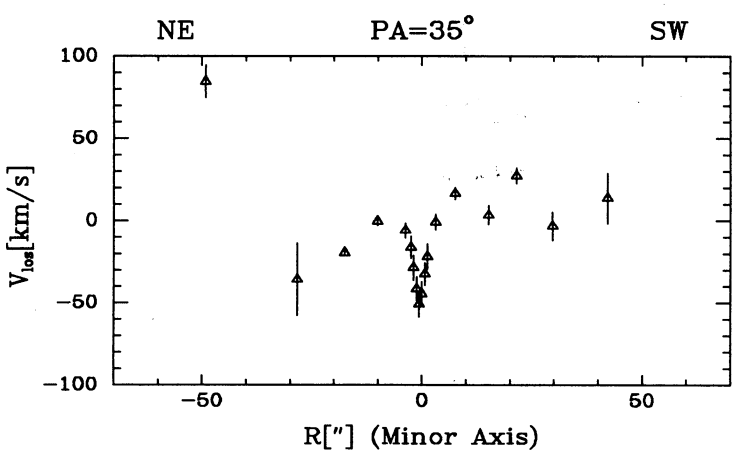

FIG. 7.—This figure displays the kinematics of the ionized gas along the minor axis (P.A. = 35°), as derived from Hβ and [O III] only. The sharp central dip is due to the offset between the kinematic center and the photometric center. A small amount of minor axis rotation (~30 km s^{-1}) is present. The velocity jump by 140 km s^{-1} at −50″, corresponding to about 100″ along the major axis, is in agreement with Rubin's (1994) data along P.A. = 25°.

excitation of this gas due to the uncertain effects of stellar Hβ absorption on the [O III]/Hβ ratio.

The spectra of the five H II regions are characteristic of low-excitation regions, with [O III]/Hβ ≤ 0.1 and [O II]/Hβ ≃ 0.5–1 (Oey & Kennicutt 1993) and [N II]/Hα = 0.3–0.4. These values are all typical for metal-rich H II regions (e.g., McCall, Rybski, & Shields 1985). Oey & Kennicutt (1993) estimate the abundances as roughly twice solar, based on the ([O II] + [O III])/Hβ calibration of Dopita & Evans (1986). Uncertainties in the calibration of this "empirical" abundance index at high metallicity are considerable, but the regions are certainly above solar metallicity. This is an interesting result because it indicates that the gas at this radius ($r \sim 40''$, near the outer edge of the prograde disk) has undergone significant chemical processing, and it rules out a heavy contamination by low-metallicity gas in this region.

Figure 8 shows the run of Hα, [N II] λ6583, and [O I] λ6300 equivalent widths (eastwest) along the major axis, as well as the variation in [N II] λ6583/Hα and [S II] λλ6717, 6731/Hα line ratios. Outside of the nuclear region ($-5'' < R < 5''$), the line ratios show a correlation with the H II kinematics. Where the ionized gas streams at $\sim v_c$ in the prograde direction ($10'' < R < 30''$ in the southeast and $-60'' < R < -10''$ in the northwest), these ratios are consistent with photoionized gas (Osterbrock 1989) and the ratios found in the H II regions (Oey & Kennicutt 1993). In the transition region, in particular $30'' < R < 65''$ in the southeast, both the [S II]/Hα ratios (∼0.5–1) and the [N II]/Hα ratios (∼0.8–1.8) indicate highly excited gas. The fractional error in these ratios, due to imperfect correction for the underlying Hα absorption, is only about 25%. However, in light of the high gas velocity dispersions (∼65 km s^{-1}) measured in that region, these line ratios might be attributed to shock excitation. The shock models shown in Ho, Filippenko, & Sargent (1993) predict [N II]/Hα and [S II]/Hα to be about unity for shocks of ∼100 km s^{-1}, roughly consistent with the values found for NGC 4826. These same models also predict [O I] λ6300/Hα = 0.1–0.3. Even though we do not detect [O I] beyond 20″ from the center, our upper limits appear consistent with the shock prediction. The line ratios show the same correlation with the gas kinematics in the northwest portion of the transition region $R < -60''$. This nonstellar excitation makes it difficult to place firm limits on the chemical composition of the outer gas disk, though the presence of strong [N II] and [S II] emission appears to rule out extremely low abundances.

6.2. *Nuclear Gas*

The nuclear region of NGC 4826 has been classified as a LINER (Heckman, Balick, & Crane 1980; Keel 1983; Filippenko & Sargent 1985), because of its typical low-ionization spectrum. Our spectrum shows strong nuclear [O I] λ6300 emission (see Fig. 8). The observed line ratio [O I]/Hα = 0.08 meets the LINER criterion defined by Osterbrock (1989): [O I]/Hα > 0.05. Even though Hα at the nucleus is weaker than in the surrounding (3″) region, it is characterized by [N II]/Hα ratios slightly above 2, higher than found elsewhere.

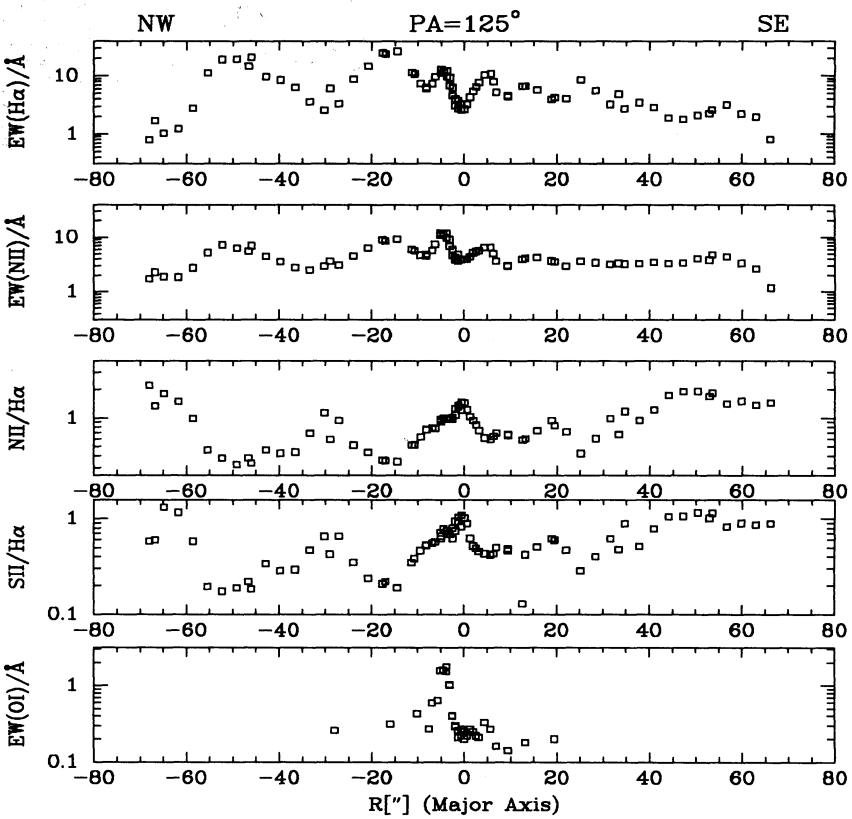

FIG. 8.—The five panels show the equivalent widths (EW) and line ratios of several diagnostic emission lines along the major axis of NGC 4826. All line fluxes were measured after correcting the spectra for the underlying stellar absorption features (see §§ 3.2 and 3.3). Residual systematic errors in the Hα eastwest are estimated to be ∼0.5 Å and ∼0.2 Å in the other lines. The properties of the disk gas ($|R| \gtrsim 10''$) are described in § 6.1. The nuclear gas and the possible supernova remnant at $R = -4''.5$ (Note the O I emission peak in the bottom panel!) are discussed in § 6.2.

Even though we detected [O I] emission at the optical center, it has a distinct peak in a region of enhanced Hα emission 4″ to 5″ northwest from the nucleus on the major axis (Fig. 8). Interestingly, this region coincides with the peak of the radio emission in the 1.″3 VLA image of NGC 4826 presented by Hummel et al. (1987). A similar Hα knot on the southeast side of the nucleus shows much less [O I] (by a factor of 5–10) and does not contain a bright discrete radio source. The optical (Braun et al. 1994) and kinematic centers are clearly offset from the radio source, and it appears unlikely that the latter is the actual center of NGC 4825.

The presence of [O I], the discrete radio knot, and the off-center location suggest that we may be seeing a supernova remnant (SNR). There is weak [N I] λ5200 emission on this location, in agreement with this interpretation. We list some parameters for this source in Table 2. The radio knot appears unresolved, implying a size less than 25 pc. The Hα knot has a FWHM of 3.5 pixels or 50 pc, similar to the extent of the [O I] emission. The spectral signature of the region is in good agreement with that expected from a SNR (e.g., Blair, Kirshner & Chevalier 1981). However, the radio and Hα luminosities are quite high for a single SNR. In particular, the knot in NGC 4826 is about 6 times brighter in Hα than the brightest remnant found in M31, and some 40 times brighter in the radio than the brightest Galactic forbidden-line SNR (Braun & Walterbos 1993). This, together with the difference in radio and optical size, suggests that the knot is possibly a complex of SNRs, with a range in ages. The radio luminosity is comparable to that of Cas A, a young SNR, while the optical size and the forbidden-line ratios suggest a much older SNR. Considering the star formation activity in this region, it is perhaps not implausible to find multiple remnants close together. The presumably dense interstellar environment may also produce bright emission from SNRs here. On the other hand, the properties of the object are very similar in several aspects to a bright single SNR in NGC 6946, recently discussed by Blair & Fesen (1994). Generally, LINER spectra are associated with weak AGNs (Osterbrock 1989), but it seems that at least part of the circumnuclear region in NGC 4826 can be more easily interpreted in a supernova/shock model.

7. DISCUSSION AND CONCLUSIONS

The main observational results of this present study of NGC 4826 can be summarized as follows.

1. The analysis of high-quality absorption-line spectra along the principal axes of NGC 4826 shows that, despite the peculiar gas kinematics, the stellar kinematics are perfectly "normal": the rotation speed of the stars rises rapidly to a local maximum at 3″, reaches its asymptotic value at 50″ ($\sim R_{exp}$), and remains flat thereafter out to the last measured point at 135″.

2. Inside 50″ the stellar velocity dispersion is roughly constant at ~ 90 km s^{-1} and then drops, reacing ~ 30 km s^{-1} at 130″. This behavior is similar to the stellar kinematics found in other disk galaxies (e.g., Fillmore, Boroson, & Dressler 1986; van der Kruit & Freeman 1986; Bottema 1992). Likewise optical surface photometry of the disk shows a relatively undisturbed exponential profile, apart from the prominent dust lane at $r \sim 40''$ (Walterbos et al. 1994).

3. Along the major axis we analyzed the stellar velocity profile in detail, searching for counterstreaming stars at radii greater than 70″. No such stars were detected. Instead, we derived an upper limit of 5% on the fraction of stars in the disk that could be counterstreaming at radii $70'' < r < 130''$. This upper limit corresponds to a stellar mass of $\lesssim 2 \times 10^8\ M_\odot$.

4. Inside $\sim 40''$ the ionized (and neutral) gas was found to rotate in the same sense as all the stars. At large radii the sense of rotation reverses, consistent with the H I velocity field and the ionized gas kinematics measured by Rubin (1994). Therefore it is the outer gas disk that is in counterrotation with respect to the galaxy.

5. The transition from prograde to retrograde rotation in the gas is not abrupt, but extends over at least 600 pc in radius. Unfortunately, our emission-line data do not cover the whole transition region. There are significant and gross asymmetries between the northeast and southeast side. Over an extended region ($\gtrsim 20''$) on the southeast side there is gas with ($v_{proj} \ll v_{circ}$), but a large (~ 65 km s^{-1}) velocity dispersion. The kinematics of the transition region cannot be fully explained by any stationary model, even if we allow for a warp or inflow.

6. NGC 4826 differs from NGC 4550 and NGC 7217 (which contain counterrotating stellar disks) in two important respects: first, in NGC 4826 the fraction of counterrotating mass is at least an order of magnitude lower than in the other two examples. Second, all detected counterstreaming material is gas; no counterrotating stars were detected.

7. The kinematic center of the galaxy is offset by $\sim 1''$ from the brightest region at 5000–6500 Å. The most likely explanation for this offset is that the true galaxy nucleus is obscured by dust at visible wavelengths. This is confirmed by infrared imaging of the nucleus (Block et al. 1994).

8. The H II regions near the outer edge of the inner gas disk are metal-rich, with oxygen abundances above solar (Oey & Kennicutt 1993; this paper). The ionized gas in the transition region shows strong [S II] and [N II] emission and may be shock-excited. The circumnuclear region also exhibits strong [N II] and [S II] emission, there probably related to the LINER nucleus and supernova activity.

As outlined in the Introduction, the existence and frequency of disk galaxies containing material of discrepant spins may provide important empirical clues to disk formation. We may ask what these new data imply for the formation history of

TABLE 2

PROPERTIES OF THE POSSIBLE SNR AT $R = -4''$

Property	Value	Notes
Hα luminosity	10^{38} ergs s^{-1}	No extinction correction
Hα/Hβ	4.2	No extinction correction
[O III](5007 Å)/Hβ	1.2	
[N I](5200 Å)/Hβ	0.4	
[N II](6584 Å + 6548 Å)/Hα	1.2	
[S II](6716 Å + 6731 Å)/Hα	1.0	
Power at 1.4 GHz	4.2×10^{25} ergs s^{-1} Hz^{-1}	

NGC 4826 and for the assembly of disks in general? For the specific case of NGC 4826, the stellar kinematics indicate that the galaxy has not been subject to recent violent relaxation, because there is no evidence for strong heating of the disk. The azimuthal velocity dispersion, measured from the major axis data, and the radial velocity dispersion, measured from the minor axis data, at 2–3 exponential scale lengths are as low as in other disk galaxies (e.g., van der Kruit & Freeman 1986; Bottema 1992). These observations lead us to conclude that NGC 4826 has not undergone a merger with another galaxy of significant size since the formation of its stellar disk. More quantitatively, a comparison with the disk heating found at $3R_{exp}$ in the N-body simulations of Quinn, Hernquist, & Fullagar (1993) indicates that any merged companion must have had a mass $\lesssim 0.1$ that of the main galaxy. This inference is further supported by the fact that the upper mass limit on counterrotating stars is only a few percent of its total stellar mass. The mass of any counterrotating stars at $R \geq 70''$ is at most comparable to the measured mass of the counterrotating H I. Since luminous galaxies at the present epoch have more stellar mass than H I mass (Roberts & Haynes 1994), there are relatively few candidate galaxies for such a merger available in the nearby universe. However, a very gas rich dwarf galaxy with $M(\mathrm{H\ I}) \sim M(\mathrm{stars}) \sim 2 \times 10^8\ M_\odot$ would constitute a feasible candidate, with its stars eluding detection.

Finally, the stellar kinematic data support the inference that the inner and outer H I disks are coplanar with the stellar disk (to within $\lesssim 10°$). All these facts point toward most of NGC 4826 being now in a steady state ($t_{evol} > t_{orb}$) and a formation scenario which is different from a galactic merger, i.e., different from the coalescence of two comparably sized, predominantly stellar galaxies within a few dynamical periods (e.g., Hernquist & Barnes 1992).

Envisioning the formation of NGC 4826 through the capture and infall of H I gas or a gas-rich dwarf galaxy with retrograde spin would explain a number of the observed features naturally: (1) it explains the absence of any observable amount of counterrotating stars in the disk. (2) The *total* acquired mass may be only a few times $10^8\ M_\odot$ and hence leave the galaxy undisturbed, independent of whether it had been acquired slowly or on a dynamical timescale. (3) The dissipative nature of the gas will eventually make it coplanar with the stellar disk, even if the accretion occurred at a skew angle.

In this scenario NGC 4826 may be more analogous to polar rings, where gas (and some stars) with discrepant angular momentum orbits around a galaxy in a steady state, rather than a violent (massive) merger. NGC 4826 is manifest proof that the H I gas, if acquired as disk-building material over a sizable fraction of a spiral galaxies age, need not always have the same sense of rotation as the rest of the galaxy.

However, this scenario raises several vexing questions of its own. If the counterrotating gas disk in NGC 4826 is the result of slow accretion of gas clouds or the coalescence of a gas-rich companion on retrograde orbit, why are such H I disks not seen elsewhere? Counterrotating disks of ionized gas have been observed in a number of early-type (S0, S0/a) galaxies (e.g., Bertola et al. 1992), but in most of those cases the counterrotating gas is concentrated in the nuclear region of the galaxy. Are H I disks like those in NGC 4826 rare, and if so, why?

The kinematics of the transition region between the counterrotating gas disks ($r \sim 50''$–$100''$) are also difficult to reconcile with the regular H I distribution and velocity field of the outer disk. The settling time for the outer disk, for example at $R = 15$ kpc, is $t_{age} \lesssim$ few $t_{orb} \sim 1$ Gyr. If we are correct in interpreting the rotation curve in a (roughly) coplanar geometry, some of the gas in this transition region is on almost radially infalling orbits (cf. Braun et al. 1994; Rubin 1994) and some of it experiences significant pressure support (this paper). This may be difficult to produce by any viscous process which gradually ($J/\dot{J} > t_{orb}$) removes angular momentum, J, from the outer gas disk (Braun et al. 1994). To the contrary, the existence of infalling gas would argue for significant evolution in the gas disk on a dynamical timescale ($< 10^8$ yr), belying the apparently regular structure and kinematics of the outer H I disk.

Another interesting question is the fate of the original *prograde* gas that is likely to have existed originally in NGC 4826. In most normal Sa–Sb galaxies the bulk of the H I gas lies at radii comparable or larger than the optical radius of the galaxy. We detect no such prograde H I or ionized gas beyond $r \sim 1$–1.5 kpc in NGC 4826 today. Presumably any such gas would have suffered inelastic collisions with the retrograde disk and would have gradually lost angular momentum and spiraled into the center of the galaxy. This mechanism offers an elegant explanation for the abnormally high gas surface densities in the center of NGC 4826 (Braun et al. 1994) and might as well account for the peculiar kinematics of the gas in the transition region.

The authors gratefully acknowledge enlightening discussions with D. Friedli, P. Sackett, L. Sparke, and J. van Gorkom. The referee, Vera Rubin, provided many helpful comments, which greatly improved the presentation of the results. H. W. R. was supported by a Hubble fellowship (HF-1024.01-91A), R. C. K. was supported by the NSF through grant AST 90-19150, and R. A. M. W. acknowledges support from NSF grant AST 91-23777.

APPENDIX

Tables 3 and 4 present data for stars and ionized gas at different position angles.

TABLE 3

STARS

R	V (km s^{-1})	ΔV	σ (km s^{-1})	$\Delta\sigma$	R	V (km s^{-1})	ΔV	σ (km s^{-1})	$\Delta\sigma$
Major Axis SE (P.A. = 125°)									
NW:									
−10.″7	59.2	3.5	91.3	4.4	5.0	−47.8	3.8	105.8	4.4
−8.8	62.8	4.2	94.8	4.4	6.3	−42.8	2.8	111.4	3.4
−7.6	67.2	3.5	100.0	3.7	7.6	−41.0	3.6	113.2	4.1
−6.3	71.5	2.4	97.1	3.7	8.8	−43.8	3.3	106.2	5.1
−5.7	71.3	3.9	94.4	4.1	10.1	−44.2	2.9	105.4	3.4
−5.0	71.1	3.2	94.1	3.4	12.0	−49.9	3.7	107.6	3.7
−4.4	67.2	3.4	93.7	3.4	13.9	−51.8	3.9	104.2	4.4
−3.8	63.7	2.8	91.8	3.0	16.4	−60.1	3.3	104.4	4.4
−3.2	50.0	2.6	95.6	2.7	18.9	−63.6	3.6	105.5	4.4
−2.5	35.3	2.4	100.9	2.7	22.0	−66.5	4.4	115.9	4.4
−1.9	23.2	1.6	96.5	2.4	25.8	−71.9	3.6	98.8	5.4
−1.3	13.0	1.9	98.0	1.7	30.2	−78.9	3.6	109.8	4.7
−0.6	4.0	1.5	95.5	2.0	35.3	−89.0	3.0	100.1	3.7
0.0	−4.4	2.4	93.5	1.7	41.0	−104.3	2.9	87.0	4.4
0.6	−15.8	1.3	93.2	1.7	47.2	−107.5	2.5	60.0	4.4
1.3	−24.2	1.7	93.2	2.0	54.8	−117.9	3.2	53.0	4.4
1.9	−33.5	1.7	98.6	1.7	64.3	−123.0	2.5	43.2	4.7
2.5	−42.1	2.2	98.9	2.4	75.6	−121.5	2.4	40.7	3.7
3.2	−45.6	2.7	100.1	3.4	89.5	−124.9	2.2	47.7	4.1
3.8	−47.1	2.7	102.2	3.7	104.6	−119.7	3.0	41.6	6.1
4.4	−44.8	3.3	102.6	3.7	134.8	−120.9	12.0	20.2	17.3
					SE:				
Major Axis NW (P.A. = 125°)									
NW:									
−127.9	113.3	4.8	32.7	7.4	−3.8	67.2	1.8	82.7	3.0
−111.5	122.4	4.1	34.9	6.1	−3.2	56.2	1.8	86.5	3.4
−96.4	124.4	2.7	37.9	3.4	−2.5	43.3	1.9	89.8	2.4
−81.3	125.0	2.4	49.5	3.0	−1.9	31.1	2.3	90.7	2.0
−68.7	120.6	2.2	48.0	4.1	−1.3	16.8	1.5	89.4	1.7
−59.2	117.6	2.6	50.3	4.1	−0.6	1.9	0.8	88.3	1.1
−51.7	114.4	3.1	57.7	4.1	0.0	−5.8	1.5	85.6	2.7
−45.4	111.0	3.1	67.2	5.1	0.6	−15.6	1.1	88.6	2.0
−39.7	106.6	3.2	83.7	4.4	1.3	−25.8	1.9	90.9	1.7
−33.4	97.8	3.3	90.0	4.7	1.9	−37.4	1.9	91.7	2.7
−28.4	87.5	3.2	82.4	4.7	2.5	−45.7	1.9	91.6	2.7
−23.9	81.8	3.4	97.8	3.7	3.2	−50.0	2.0	91.9	2.7
−19.5	66.7	3.7	102.1	5.4	3.8	−49.5	3.2	97.1	3.4
−16.4	68.2	3.8	98.9	5.1	4.4	−50.4	3.2	96.6	3.7
−13.2	54.1	2.9	95.9	3.7	5.0	−48.5	2.8	99.6	3.7
−10.7	57.1	3.7	97.1	3.4	6.3	−42.6	2.8	100.9	3.4
−8.8	54.6	4.2	95.0	4.4	7.6	−37.2	3.3	105.6	4.1
−7.6	59.5	3.5	95.9	4.4	8.8	−37.9	4.0	104.4	4.1
−6.3	66.0	3.1	95.2	3.4	10.1	−36.6	3.6	99.4	3.7
−5.7	72.0	3.5	83.9	4.4	12.0	−45.1	3.6	102.1	3.7
−5.0	76.3	3.0	81.6	3.7	13.9	−49.2	3.2	99.2	4.4
−4.4	72.9	3.3	80.5	2.7	SE:				
Minor Axis (P.A. = 35°)									
NE:									
−59.8	−12.0	5.6	45.0	8.5	2.5	−4.4	2.0	106.4	2.3
−44.7	−10.2	4.7	76.6	5.4	3.8	−6.3	2.9	104.1	3.0
−29.6	−27.2	3.0	61.2	3.9	5.0	−4.2	3.0	119.0	3.3
−14.5	−18.6	5.4	95.9	6.7	7.6	2.4	3.0	118.7	3.5
−5.0	−27.4	3.2	90.5	3.8	11.3	9.1	3.3	92.1	3.8
−1.9	−32.4	1.7	87.5	2.4	17.6	8.4	3.2	95.6	3.4
−1.3	−26.1	1.7	93.1	2.0	27.1	13.9	3.0	72.4	3.9
−0.6	−22.5	1.3	97.3	1.7	41.0	15.8	3.2	44.1	4.4
0.0	−17.0	1.5	94.0	1.8	56.1	16.7	4.1	36.2	6.7
0.6	−13.9	1.6	96.6	2.0	71.2	25.7	7.6	31.7	10.8
1.3	−9.2	2.2	95.8	2.6	SW:				

TABLE 4

A. Ionized Gas (Hα, N II, S II)

R	V (km s^{-1})	ΔV	σ (km s^{-1})	Δσ	R	V (km s^{-1})	ΔV	σ (km s^{-1})	Δσ
Major Axis SE (P.A. = 125°)									
NW:									
−9.4.....	113.1	2.0	37.2	2.6	12.6.....	−135.1	2.0	35.1	2.7
−6.9.....	102.1	2.0	45.7	2.1	15.8.....	−138.7	2.0	45.2	2.1
−5.0.....	101.4	2.0	62.2	1.5	18.9.....	−133.2	2.0	53.2	1.9
−3.8.....	90.3	2.0	72.7	1.3	22.0.....	−140.3	2.0	39.1	2.5
−3.2.....	81.6	2.0	72.9	1.3	25.2.....	−143.0	2.0	33.1	2.9
−2.5.....	66.9	2.0	75.2	1.3	28.4.....	−149.5	2.0	36.6	2.9
−1.9.....	39.5	2.0	85.4	1.3	31.5.....	−135.4	3.9	64.3	3.7
−1.3.....	7.1	2.0	91.8	1.9	34.7.....	−110.1	5.2	77.7	4.5
−0.6.....	−29.2	2.0	92.8	1.6	37.8.....	−98.7	3.9	63.2	4.0
0.0.....	−53.5	2.0	82.1	1.3	41.0.....	−90.3	4.6	66.5	4.2
0.6.....	−69.7	2.0	70.1	1.4	44.1.....	−85.2	7.9	74.0	8.0
1.3.....	−77.9	2.0	59.7	1.6	47.2.....	−70.5	11.8	45.1	13.0
1.9.....	−87.9	2.0	49.1	2.0	50.4.....	−52.9	6.5	60.1	5.6
2.5.....	−96.5	2.0	45.7	2.1	53.5.....	−35.0	3.9	55.7	5.6
3.2.....	−103.8	2.0	47.6	2.0	56.7.....	−16.9	6.5	68.5	6.6
4.4.....	−116.8	2.0	51.0	1.9	59.8.....	−15.2	9.2	74.7	9.3
5.7.....	−117.4	2.0	46.6	2.1	63.0.....	−20.1	9.1	48.1	9.5
6.3.....	−120.4	2.0	41.3	2.3	66.2.....	−22.6	15.1	44.0	24.1
9.4.....	−115.6	2.0	37.7	2.5	SE:				
Major Axis NW (P.A. = 125°)									
NW:									
−67.4.....	114.6	16.2	46.1	39.2	−20.2.....	133.6	2.0	28.3	3.4
−64.3.....	121.0	8.6	36.7	15.1	−17.0.....	122.7	2.0	27.0	3.6
−61.1.....	136.8	13.7	27.0	18.6	−13.9.....	118.8	2.0	27.1	3.5
−58.0.....	123.4	3.2	23.5	6.4	−10.7.....	118.7	2.0	33.1	2.9
−54.8.....	122.5	2.0	11.9	8.1	−7.6.....	104.7	2.0	34.8	2.8
−51.7.....	126.2	2.0	16.4	5.9	−5.7.....	103.6	2.0	49.8	1.9
−48.5.....	122.2	2.0	17.4	5.5	−4.4.....	99.0	2.0	67.5	1.4
−45.4.....	123.8	2.0	14.8	6.5	−3.8.....	93.4	2.0	81.8	1.2
−42.2.....	114.4	2.0	22.6	4.2	−3.2.....	86.6	2.0	80.6	1.2
−39.1.....	107.7	2.0	25.6	3.8	−2.5.....	76.0	2.0	73.8	1.3
−35.9.....	104.3	2.0	25.6	4.2	−1.9.....	58.1	2.0	78.0	1.3
−32.8.....	98.2	2.3	33.8	3.4	−1.3.....	18.5	2.0	91.8	1.3
−29.6.....	109.4	2.6	43.6	3.4	−0.6.....	−24.6	2.0	105.1	1.3
−26.5.....	118.5	2.1	36.0	3.4	0.0.....	−28.4	2.0	96.4	1.3
−23.3.....	136.2	2.0	28.0	3.4	SE:				

TABLE 4

B. Ionized Gas (Hβ, O III)

R	V (km s^{-1})	ΔV
Minor Axis (P.A. = 35°)		
NE:		
−49.1.....	84.5	9.7
−28.4.....	−36.0	22.0
−17.6.....	−19.6	2.0
−10.1.....	−0.4	2.5
−3.8.....	−6.0	4.1
−2.5.....	−16.3	6.6
−1.9.....	−28.8	7.6
−1.3.....	−41.6	7.1
−0.6.....	−50.9	7.7
0.0.....	−44.6	7.1
0.6.....	−32.6	6.7
1.3.....	−21.9	7.6
3.2.....	−0.9	4.6
7.6.....	16.4	3.6
15.1.....	3.4	5.6
21.4.....	27.2	4.6
29.6.....	−3.4	8.7
42.2.....	13.5	15.2
SW:		

REFERENCES

Barnes, J. E., & Hernquist, L. E. 1992, ARA&A, 30, 705
Bertola, F., Buson, L., & Zeilinger, W. 1992, ApJ, 401, 79
Bettoni, D., Galletta, G., & Osterloo, T. 1991, MNRAS, 248, 544
Binney, J., & May, A. 1986, MNRAS, 218, 734
Binney, J., & Tremaine, S. 1987, Galactic Dynamics (Princeton: Princeton Univ. Press)
Blair, W. P., & Fesen, R. A. 1994, ApJ, 424, L103
Blair, W. P., Kirshner, R. P., & Chevalier, R. A. 1981, ApJ, 247, 879
Block, D., Witt, A. N., Grosbol, P., & Stockton, A. 1994, A&A, in press
Bottema, R. 1992, A&A, 257, 69
———. 1993, A&A, 275, 16
Bothun, G. 1985, AJ, 90, 1982
Braun, R., & Walterbos, R. A. M. 1993, A&AS, 98, 327
Braun, R., Walterbos, R., & Kennicutt, R. 1992, Nature, 360, 442
Braun, R., Walterbos, R., Kennicutt, R., & Taconi, L. 1994, ApJ, 420, 558
Casoli, F., & Gerin, M. 1993, A&A, 279, L41
Dopita, M. A., & Evans, I. N. 1986, ApJ, 307, 431
Filippenko, A., & Sargent, W. 1985, ApJS, 57, 503
Fillmore, J., Boroson, T., & Dressler, A. 1986, ApJ, 302, 208
Heckman, T. M., Balick, B., & Crane, P. C. 1980, A&AS, 40, 295
Ho, L., Filippenko, A., & Sargent, W. 1993, ApJ, 417, 63
Hummel, E., van der Hulst, J. M., Keel, W. C., & Kennicutt, R. C. 1987, A&AS, 70, 517
Katz, N. 1992, ApJ, 391, 502
Keel, W. C. 1983, ApJ, 268, 632
Kennicutt, R. C. 1983, ApJ, 272, 54
———. 1989, ApJ, 344, 685
McCall, M., Rybski, P., & Shields, G. 1985, ApJS, 57, 1
Merrifield, M., & Kuijken, K. 1994, ApJ, in press
Oey, M. S., & Kennicutt, R. C. 1993, ApJ, 411, 137
Osterbrock, D. E. 1989, Astrophysics of Gaseous Nebulae and Active Galactic Nuclei (Mill Valley, CA: Univ. Science Books)
Quinn, T., & Binney, J. 1992, MNRAS, 255, 729
Quinn, P., Hernquist, L., & Fullagar, D. P. 1993, ApJ, 403, 74
Rix, H.-W., Franx, M., Fisher, D., & Illingworth, G. 1992, ApJ, 400, L5
Rix, H.-W., & White, S. D. M. 1992, MNRAS, 254, 389
Roberts, M. S., & Haynes, M. P. 1994, ARA&A, in press
Rubin, V. 1994, AJ, 107, 173
Rubin, V., Graham, J., & Kenney, D. 1992, ApJ, 394, L9
Sandage, A., & Tammann, G. A. 1981, A Revised Shapley Ames Catalog of Galaxies (Washington: Carnegie Institution)
Toomre, A. 1982, ApJ, 259, 535
van der Kruit, P., & Freeman, K. 1986, ApJ, 303, 556
van Driel, W., & Buta, R. 1993, PASJ, 45, 47
Walker, M. F. 1989, PASP, 101, 333
Walterbos, R., Braun, R., & Kennicutt, R. 1994, AJ, 107, 184
Witt, A. N., Lindell, R. S., Block, D. L., & Evans, R. 1994, ApJ, in press